

Long-range multipartite entanglement near measurement-induced transitions

Sebastien J Avakian,^{1,2} T. Pereg-Barnea,¹ and William Witczak-Krempa^{2,3,4}

¹*Department of Physics, McGill University, Montréal, QC, Canada H3A 2T8*

²*Département de Physique, Université de Montréal, Montréal, QC, Canada H3C 3J7*

³*Centre de Recherches Mathématiques, Université de Montréal, Montréal, QC, Canada H3C 3J7*

⁴*Institut Courtois, Université de Montréal, Montréal, QC, Canada H2V 0B3*

Measurements profoundly impact quantum systems, and can be used to create new states of matter out of equilibrium. Here, we investigate the multipartite entanglement structure that emerges in quantum circuits involving unitaries and measurements. We describe how a balance between measurements and unitary evolution can lead to multipartite entanglement spreading to distances far greater than what is found in non-monitored systems, thus evading the usual fate of entanglement. We introduce a graphical representation based on spanning graphs that allows to infer the evolution of genuine multipartite entanglement for general subregions. We exemplify our findings on circuits that realize a 1d measurement-induced dynamical phase transition, where we find genuine 3-party entanglement at all separations. The 2- and 4-party cases are also covered with examples. Finally, we discuss how our approach can provide fundamental insights regarding entanglement dynamics for a wide class of quantum circuits and architectures.

Introduction—Measurements profoundly impact quantum systems, especially their quantum entanglement. A perfect measure of a spin’s component collapses its wavefunction into a pure state un-entangled with other parts of the system. Such a loss of entanglement can actually promote entanglement among the remaining degrees of freedom of the system as they become “liberated” from the measured spin. But the decoupling of the measured spin is only temporary, since being in a pure product state, it is very “entangleable,” namely it can be readily entangled with its environment. In contrast, a highly mixed (decohered) spin would not be entangleable. We thus see that measurements can have highly non-trivial effects on the entanglement structure in quantum many-body systems. Partial monitoring involving measurements on parts of a system can be used to reach new non-equilibrium regimes beyond what is possible in usual unitary evolution. An example is the appearance of measurement-induced dynamical phase transitions in quantum circuits with unitary and measurement layers, Fig. 1. It was observed that as one increases the measurement rate, a continuous transition from a volume law for the von Neumann entanglement entropy to an area law occurs [1–7]. A finer analysis of the bipartite entanglement yielded the numerical observation that the critical point has a logarithmic negativity [8, 9] for two intervals that decays algebraically with separation (after ensemble averaging) [10]. Such long-range entanglement is striking given that quantum matter at equilibrium will typically have short-ranged entanglement, both bipartite and multipartite, owing to the fate of entanglement under general types of evolution, both in space and time [11]. A striking example can be found in quantum critical groundstates described by conformal field theories where the bosonic logarithmic negativity between separated subregions decays faster than any power in one [12, 13]

and higher dimensions [14].

In this work, we investigate the multipartite entanglement structure in general quantum circuits involving unitaries and measurements. We explain how a balance between measurements and unitary evolution can lead to multi-party entanglement spreading to distances far greater than what is found in non-monitored systems. We introduce a graphical representation that allows to identify the evolution of multipartite entanglement structure, and exemplify it on simple circuits. We support our analysis by computing measures of genuine multipartite entanglement (GME) for various subregions. In essence, GME is a collective form of entanglement that involves all parties. As the key example, we study 3-spin GME near the measurement-induced transition in 1d random Haar circuits, where we find GME at all separations. We then analyze the layer-by-layer dynamics and show how unitaries and measurements work in tandem to produce collective entanglement. We end by introducing *minimal spanning graphs* connecting the various parties, and show how these provide a framework to reveal GME in a large family of quantum circuits.

Multipartite entanglement has been studied in the monitored quantum Ising chain through the quantum Fisher information. It was found that the latter detects the measurement-induced transition [15, 16]. In contrast to our work, the Fisher information was computed for the entire chain, and could not reveal the structure of GME for subregions.

Evading the fate of entanglement—Let us look into the time evolution of a discrete quantum circuit, a simple 1d example is shown in Fig. 1. The general circuits under consideration are composed of unitary operators (boxes) that act on a group of nearby sites, and projective measurements (circles). Our goal is to understand the evolution of multipartite entanglement within general subregions. Such a subregion A is composed of m

groups of spins, A_1, \dots, A_m , and can thus possess up to m -party entanglement. We will see how the right amount of measurements can allow the system to evade the typical fate of entanglement [11].

Measurements tend to decrease the amount of collective entanglement in the entire system since the measured spins factorize from the rest. However, they can increase multipartite entanglement within A by removing entanglement to the spins in the complement, B . Indeed, if a spin in B is entangled with A , but is hit by a measurement, this entanglement will be destroyed potentially allowing more entanglement within A . This follows from monogamy: a spin in A that is strongly entangled with B cannot maximize its entanglement with other spins in A . In contrast, if a measurement hits a spin in A , this spin will no longer contribute to the entanglement within A .

Unitaries generate the entanglement in the first place. Consider a product state of 2 spins acted upon by a unitary gate. The resulting state will generically be entangled. However, successive applications of the unitary will not increase entanglement indefinitely: decrease will eventually occur. Turning to a general subregion A , a degradation of entanglement will occur if various unitaries act upon the subregion without being interrupted by measurements due to scrambling. In fact, measurement-free unitary evolution will typically drive A towards and into the separable space of states [11]. We thus see that a balance between measurements and unitaries must be achieved to allow entanglement to spread.

The inset of Fig. 2 schematically illustrates these principles. We represent the space of states on subregion A that have no entanglement, i.e. classical mixtures of product states $\rho_1 \otimes \dots \otimes \rho_m$, by a disk surrounded by a sea of entangled states. We then illustrate the typical layer-by-layer time-evolution of $\rho_A(t)$ in the regimes of low (blue), intermediate (orange), and high (green) measurement rates. At low rates, scrambling limits entanglement, and the state actually penetrates within the separable continent. At high rates, the state spends most of the time on the boundary of the separable set; that is where pure product states live. Measurements prevent ρ_A from penetrating the separable continent. At intermediate rates, measurements still prevent the state from penetrating too deep into the separable continent, allowing unitaries to generate substantial entanglement. Below we shall provide quantitative analysis that precisely supports this qualitative picture.

Multipartite entanglement spreading— We examine in more detail how multipartite entanglement spreads in quantum circuits. In particular, we want to identify subregions A that possess GME, which means that the reduced density matrix ρ_A is not biseparable. For example, in the case of three subregions $A = A_1 A_2 A_3$, a biseparable state is a mixture of states sepa-

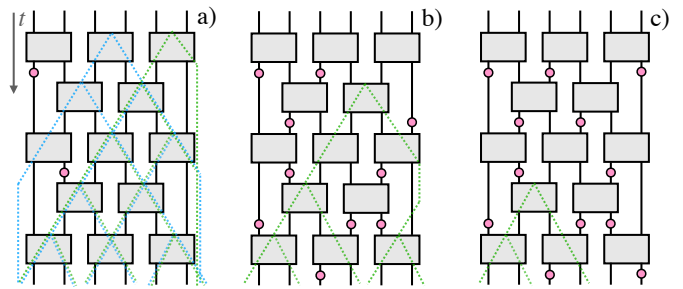


FIG. 1. **Circuits and entanglement spreading.** Three quantum circuits composed of two-site unitaries (grey boxes) and measurements (pink circles); the measurement rate increases left to right. Time flows downwards. Entanglement graphs that propagate to the final spins are shown. Different colors in (a) correspond to distinct seeds.

table under some partition:

$$\rho_{\text{bisep}} = \sum_k p_k \rho_1^k \otimes \rho_{23}^k + q_k \rho_{13}^k \otimes \rho_2^k + r_k \rho_{12}^k \otimes \rho_3^k \quad (1)$$

where $p_k, q_k, r_k \geq 0$, and the $\rho_{\#}^k$ are physical density matrices. An elementary graphical representation will allow us to visualise the evolution of the entanglement structure. We exemplify the representation in Fig. 1. Starting at the earliest times, one draws a cone of entanglement that arises from a unitary (a “seed”), as long as measurements do not prevent the cone from reaching the final state. We thus first obtain the cones with the largest spreads. For a given cone, one then draws all sub-cones that reach the final state. The procedure is repeated layer-by-layer until all possible cones are identified. The end result resembles a root system connecting the final spins, see Fig. 1. For a set of spins to be entangled, it is necessary for them to be connected by roots. However, this is not sufficient since too many overlapping root systems will scramble the spins. Indeed, different root systems possess different seeds, so that the spins connected by overlapping roots receive quantum information from independent sources, preventing them from reliably encoding the information coming from any given seed. A low rate of measurements gives many overlapping roots, with little resulting entanglement, see Fig. 1a. In contrast, a high measurement rate only allows short roots to grow, strongly suppressing the range of entanglement, as shown in Fig. 1c. For intermediate rates (Fig. 1b), one achieves a root spanning numerous sites resulting in long-range entanglement. To see which spins are entangled, one examines the sites connected by roots.

We can quantify the various form of entanglement. To do so we study the circuits in Fig. 1, and fix the unitary to be the Floquet Ising one used in Ref. [17]. The sole source of randomness arises from the probabilistic outcomes of measurements in quantum mechanics. In the regime of low measurement rate, Fig. 1a, we find no long-range GME irrespective of the measurement outcomes. For in-

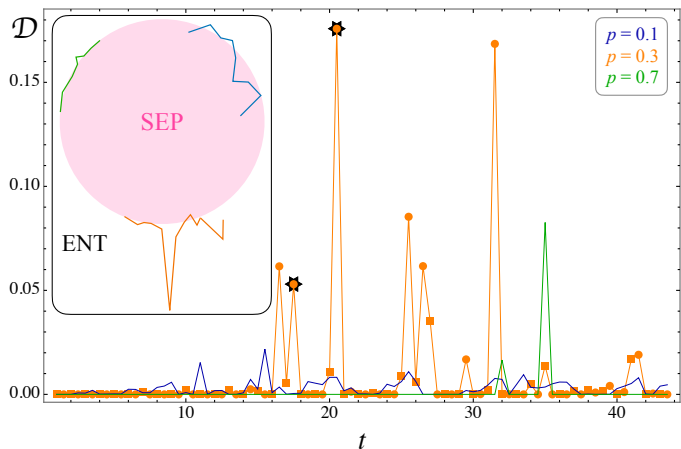


FIG. 2. **Time evolution.** The geometric entanglement, which measures the distance to SEP (inset), versus discrete time for 3 spins at positions (4, 7, 10) in a $L = 14$ chain. $\mathcal{D} > 0$ indicates the presence of bipartite or tripartite entanglement. Unitaries occur at integer times $t = 1, 2, \dots$, while measurements at $t = 3/2, 5/2, \dots$. For $p = 0.3$, post-unitary states are marked with squares, and post-measurement ones with circles. Black stars denote detection of GME. **Inset.** The separable continent (SEP) is surrounded by entangled states (ENT). Typical time evolution paths are schematically shown for the three p values.

stance, we detect no genuine tripartite entanglement between 3 sites; the same conclusion holds for 4-site GME. To reach these conclusions we use bi-separability criteria [18], the key one being

$$W = \max_{LU} |\rho_{18}| - \sqrt{\rho_{22}\rho_{77}} - \sqrt{\rho_{33}\rho_{66}} - \sqrt{\rho_{44}\rho_{55}} \quad (2)$$

which if $W > 0$ indicates that the state cannot be written as (1) and there is GME between the 3 spins. If the RHS is non-positive a conclusion cannot be reached, and we set $W = 0$. The maximisation is over all local unitary transformations on the 3-spin density matrix ρ_{ij} . We employed a similar criterion for 4-spin GME [18], W_4 , as explained in the Supplementary material (SM). Moving to the intermediate measurement rate circuit in Fig. 1b, we detect GME between sites 124 and sites 246; the former is stronger since the root system connecting the spins is shorter. We also find long-range 4-partite GME between sites 1256. Finally, in the high measurement rate regime, the only detected 3-spin GME is 124 owing to the corresponding root system in Fig. 1c. We thus see the general principles, and graphical representation of GME at work in a simple example.

Multipartite entanglement in random Haar circuits—We now turn to a family of circuits that realize a bona fide measurement-driven phase transition [1–5]. The circuit structure appears in Fig. 1, and the unitaries are chosen randomly via the Haar measure. Z -measurements are performed with a rate $0 \leq p \leq 1$. In Fig. 3 we show results for chains with $L = 18$ sites

at four values of p . We plot the biseparability criterion W for subregion A composed of $m = 3$ spins at positions $(i, i + x, i + 2x)$; the maximal possible range being $x = 8$. We have averaged over 4.23×10^5 samples for $p = 0.1, 0.3, 0.7$ and 4×10^4 samples for $p = 0.17$. The transition between volume and area-law regimes has been found to be at $p_c = 0.17$ [6]. We see that the intermediate value $p = 0.3$ shows a bigger $\langle W \rangle$ compared to the critical rate 0.17, similar to the results for the negativity [10]. For the four rates, $\langle W \rangle$ is largest for $p = 0.3$, and has long range as it extends to $x = 8$. In contrast, for $p = 0.1$ we have only detected events with $x \leq 4$. For both $p = 0.17, 0.7$, we only found events with $x \leq 6$, and the average value at $x = 6$ is many orders of magnitude smaller than for $p = 0.3$. We note that the lack of data points up to $x = 8$ for $p \neq 0.3$ is probably due to the following reasons: lack of samples, W does not capture all GME, the optimisation required to get W is most challenging for large x , where it becomes numerically demanding. We come back to this point at the end of the paper where we introduce a more powerful graphical representation that will allow us to infer the presence and strength of GME.

To appreciate the striking nature of the above results, it is important to put these into context. Let us compare with the analogous analysis for the transverse field Ising model near its quantum critical point in 1d. GME between 3 adjacent spins ($x = 1$) is detected by W , and takes its maximal value very close to the critical point [19–21]. However, as soon as the spins are not adjacent, GME has not been detected [19, 21]. This means that W vanishes for $x > 1$, in clear contrast to what we observe in monitored quantum circuits. An even more striking comparison can be made with the 2d quantum Ising model, where W is both weaker and occupies a smaller fraction of the phase diagram compared to the 1d case; it also vanishes for non-adjacent sites [21].

We end this section by noting that the open boundary conditions actually benefit GME by leading to the upturn of $\langle W \rangle$ in Fig. 3. Indeed, when the spins have a large separation x , the leftmost and rightmost ones have less neighbors to entangle with, which would lead to a reduction of GME within A . Alternatively, one can understand this as a reduction of sources of scrambling. Ignoring the data points showing an upturn, the behavior is consistent with exponential decay. A clearer exponential scaling is seen at $L = 24$ (Fig. 5, SM).

Time evolution—We quantitatively study how entanglement evolves in time layer-by-layer. To obtain a more complete characterization, we shall employ the geometric entanglement [22]

$$\mathcal{D} = \min_{\rho_{\text{sep}}} d(\rho, \rho_{\text{sep}}) \quad (3)$$

that measures the distance between ρ and the closest state ρ_{sep} in the separable continent, as pictured in the

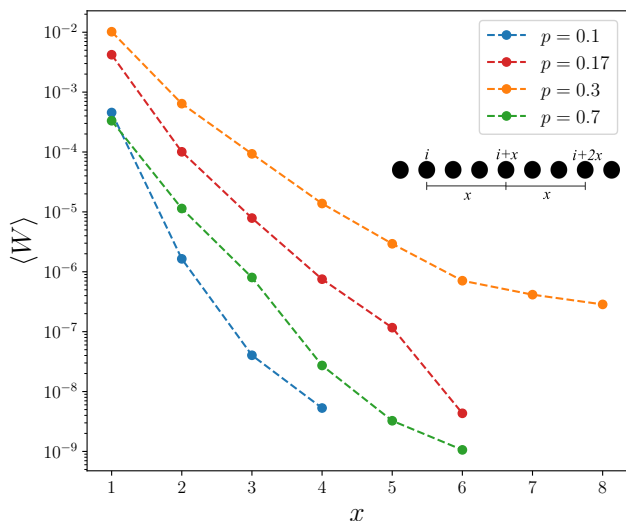


FIG. 3. **Genuine multipartite entanglement in random Haar circuits.** Log-linear plot of the ensemble average of the criterion W , Eq. (2), that detects GME among 3 spins at positions $(i, i+x, i+2x)$ in $L=18$ chains. Longer-range GME is observed for a measurement rate of $p=0.3$. For each p , the ensemble average was taken over 4×10^5 realizations for $p=0.1, 0.3, 0.7$ while for $p=0.17$ the average was taken over 4.23×10^4 realizations.

inset of Fig. 2. The strength of \mathcal{D} is that it captures all forms of entanglement. We shall use the Frobenius norm to define the Hilbert-Schmidt distance: $d(\rho_1, \rho_2) = \sqrt{\text{Tr}(\rho_1 - \rho_2)^2}$. Fig. 2 shows the time-evolution of \mathcal{D} for 3 spins at positions $(4, 7, 10)$, which corresponds to $x=2$, in a chain of $L=14$ sites. For every time t , we find the separable state of 3 spins nearest to $\rho_A(t)$, $\sum_k p_k \rho_1^k \otimes \rho_2^k \otimes \rho_3^k$ with the p_k forming a probability distribution. The numerical optimisation is done over 69 real parameters, i.e. we go up to $k=7$. We have verified numerous circuit realizations, and the ones shown represent typical behavior. We see that that \mathcal{D} remains small both at $p=0.1$ and $p=0.7$. However, at the intermediate rate $p=0.3$, \mathcal{D} exhibits recurring large spikes, meaning that ρ_A has substantial bipartite or tripartite entanglement at these times. In fact, the highest spikes occur for post-measurement states (circles). We observe the following mechanism to build a large spike: a unitary layer (square in Fig. 2) generates a small amount of entanglement in A , which is then amplified by an appropriate measurement layer (circle). In all the data shown, we only detect 3-spin GME at two times (black stars), and only for $p=0.3$. We thus see that many of the high spikes are dominated by bipartite entanglement, and possess correspondingly little or no GME.

Entanglement graphs—We wish to sharpen the graphical analysis introduced earlier to understand how GME spreads in complex monitored circuits. First, we need a more efficient representation that will allow us

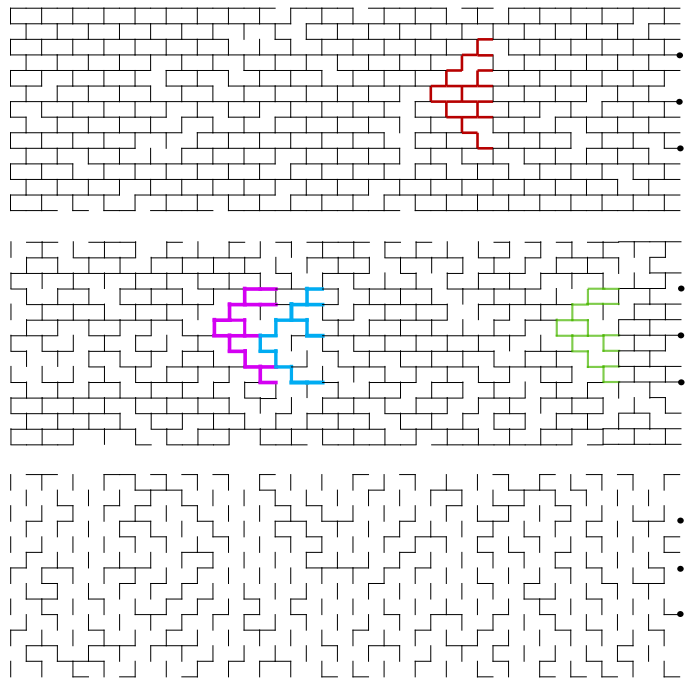


FIG. 4. **Entanglement graphs.** Quantum circuits for the $L=14$ chain described in Fig. 2. Time increases towards the right. Vertical lines are unitaries, while horizontal lines denote the absence of measurement. Top to bottom: $p=0.1, 0.3, 0.7$. The 3 spins at positions $(4, 7, 10)$ composing A are marked with black circles; their GME is discussed in the text and Fig. 2. Thicker colored bonds indicate *complete minimal spanning graphs* which are necessary but not sufficient for GME.

to tackle large systems for long times. We represent a 2-unitary by a vertical line joining the sites at equal time, and an absence of measurement by a horizontal line connecting a given site to the the next time step. This is illustrated in Fig. 4, with time increasing towards the right, for the $L=14$ circuits studied above. We want to understand the GME for a given subregion $A = A_1 \cdots A_m$ (B is the complement) by constructing entanglement graphs using the rules:

1. Find the shortest graph connecting all subregions A_1, \dots, A_m by starting from a seed and always following the arrow of time.
2. Include paths that connect this graph to other spins in B so that a *complete minimal spanning graph*, G_{\min} , is obtained. This graph translates into the following properties:
 - a) Shorter graphs tend to produce stronger entanglement;
 - b) Many B sites covered in the final state weakens entanglement within A ;
 - c) Cycles weaken entanglement (scrambling).
3. Find graphs with other seeds that touch A . If these have similar or lesser depth compared to G_{\min} , they will reduce entanglement in A .

We exemplify the construction of these graphs on the $L = 14$ circuits. The bold purple and blue graphs at $p = 0.3$ in the middle of Fig. 4 represent G_{\min} for the two times at which GME has been detected (stars in Fig. 2). We first note that both have the minimal depth required to connect sites (4,7,10). Second, G_{\min} does not cover many B sites; for the blue one, where the strongest GME has been detected, a single B site is covered. In addition, the blue graph possesses a tree structure as it has no cycles. Finally, nearby parasitic graphs that entangle A with B are limited, especially for the blue graph. In fact, the blue graph and its environment are nearly optimal. Interestingly, the purple graph occurs again at a later time, as shown in green. However, it has more parasitic graphs compared to the purple one, consistent with the fact that we detect no GME. This generalizes to the low p regime, as exemplified in the top circuit, where low depth G_{\min} occur often, but they cover many B sites. In addition, they have many parasitic graphs. An example is shown in red in the top circuit. In the case of high p , frequent measurements prevent the growth of graphs connecting distant spins, as is exemplified in the bottom circuit of Fig. 4.

The identification of G_{\min} can be applied to general subregions. For instance, in the simpler case of 2 spins, we have evaluated the logarithmic negativity $\mathcal{E}(i, j)$ between sites $i, j \in \{4, 7, 10\}$ at both times where 3-spin GME has been detected (middle circuit of Fig. 4). For all choices of pairs, we have found a non-zero answer indicating bipartite entanglement. Moreover, the graphs G_{\min} are the same as for the 3-spin case discussed in the previous paragraph, and the prediction is thus that \mathcal{E} should be larger in the blue case compared to the purple one. We have found this to be true by a good margin for the three possible choices of pairs. As a more non-trivial example we have examined the 4-spin GME in another $L = 14$ realization at $p = 0.3$ shown in Fig. 6 of the SM. We studied the GME between 4 spins in the final state belonging to the subset $\{3, 6, 8, 9, 10\}$. These spins belong to the same G_{\min} , and we have found strong GME between sites (3, 8, 9, 10) using the W_4 criterion mentioned above. Such range of 4-spin GME is much larger than what is expected in equilibrium.

The minimal spanning graphs discussed above are classical objects in spacetime, and thus fit into the quantum-to-classical framework used to study various quantities in monitored quantum circuits [7]. In particular, the graphs possess features in common with minimal cut and light cone structures [7], but are ultimately distinct. Further work is needed to understand the connection with percolation, and to determine whether entanglement graphs map to a quantitative statistical mechanical model.

Outlook— We have studied how GME dynamically evolves in quantum circuits containing measurements and unitaries. We explained how an appropriate rate of measurements can lead to strong GME between distant sub-

regions thus evading the usual fate of entanglement [11] in the scrambling regime. We have exemplified our general arguments with 1d random Haar circuits realizing a measurement-induced transition. We have found that 3-spin GME is strongest at intermediate measurement rates, and does not suffer a sudden death with separation. We have examined the dynamics in specific realizations, and identified how long-range entanglement emerges.

Most importantly, we have developed a graphical analysis based on complete minimal spanning graphs that connect the subregions. Such an approach allows to see which spins are likely to share GME. We expect that it can be used to reveal many properties about quantum circuits. For example, in the Haar circuits under study, we see that for general rates $0 < p < 1$, nearly optimal minimal spanning graphs connecting arbitrary subregions can always be constructed, although often with low probability. This means that the ensemble average of a GME measure (such as W) should not suffer a sudden death with separation. Based on the probability of the right graphs appearing, we expect the decay to be generically exponential, in line with our findings for 3 spins. The quantitative application of spanning entanglement graphs holds many promises, and future work is needed to reveal its full predictive power.

Acknowledgements— We thank Y. Hu, L. Lyu, G. Perez and R. Vasseur for useful discussions. W.W.-K. is supported by a grant from the Fondation Courtois, a Chair of the Institut Courtois, a Discovery Grant from NSERC, and a Canada Research Chair.

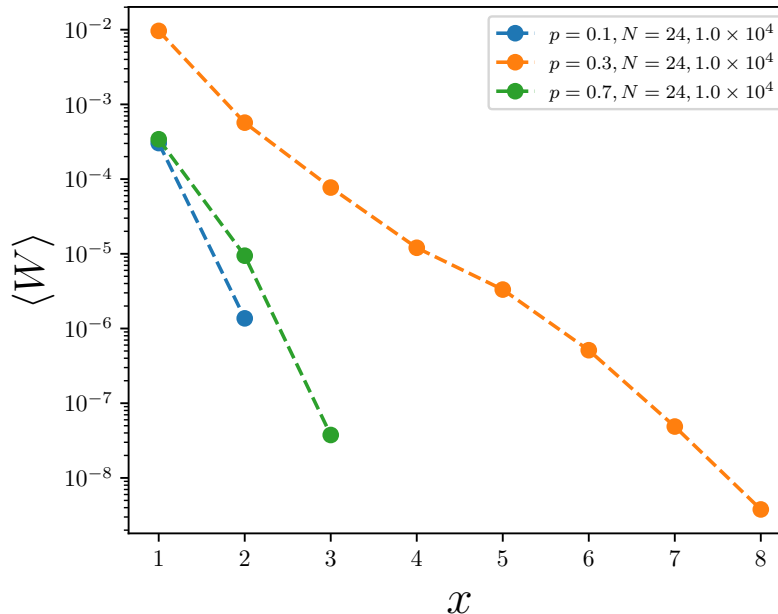


FIG. 5. **3-spin GME at $L = 24$.** Log-linear plot of the biseparability criterion W for 3 spins at positions $(i, i + x, i + 2x)$ for $L = 24$ chains. For $p = 0.1, 0.3, 0.7$, the ensemble averages occur over 10^4 realizations. For $p = 0.1$ and 0.7 positive W events are detected for $x \leq 2$ and $x \leq 3$, respectively. For 0.3 events occur for $x \leq 8$, respectively. No hits were detected for $x = 9, 10, 11$ due to the small number of realizations.

Numerics

Calculations were in part performed using Qbit++: a general high-performance quantum many-body physics simulation engine [23]. The circuit structure comprises 4 layers that are repeated [1, 7]. A first layer of unitaries is applied to the odd numbered bonds (the first consisting of the first two sites), then a measurement layer, another unitary layer on the even numbered bonds, and then another measurement layer. The unitary layers are comprised of random Haar matrices acting on two sites while the measurement layer is comprised of projective measurements in the z -basis. Each projective measurement occurs on each site with probability p . In Fig. 3, we apply a total of 98 layers, 49 unitary layers and 49 measurements layers. Note that we end with a unitary layer that covers every site (odd numbered bonds) and then a final measurement layer. The initial state is the all-0 product state in the computational basis. To obtain W for a given separation x from the final state, we obtain the reduced density of 3 spins ρ_{i_1, i_2, i_3} with $x = i_3 - i_2 = i_2 - i_1$ and optimize over local unitary transformations to extremize W . This process is repeated for every possible x in the chain. We then average over different circuit realizations in order to obtain $\langle W \rangle$ for all separations. For Fig. 3, we use a total of 4×10^5 and 4.23×10^4 circuit realizations for $p = 0.1, 0.3, 0.7$ and $p = 0.17$ respectively.

4-party genuine entanglement

We discuss examples of GME involving 4 spins obtained in the final state of the $L = 14$ circuit shown in Fig. 6. A general 4-spin state is given by a 16-by-16 density matrix with elements ρ_{ij} , $1 \leq i, j \leq 16$, where we use the standard computational basis, $\{|0 \dots 0\rangle, |0 \dots 10\rangle, \dots, |1 \dots 1\rangle\}$. The bi-separability criterion that we shall use is a close cousin of the 3-spin criterion given in the main text. It reads [18]

$$W_4 = \max_{\text{LF}} |\rho_{2,3}| + |\rho_{2,5}| + |\rho_{2,9}| + |\rho_{3,5}| + |\rho_{3,9}| + |\rho_{5,9}| - \rho_{2,2} - \rho_{3,3} - \rho_{5,5} - \rho_{9,9} \\ - \sqrt{\rho_{1,1}\rho_{4,4}} - \sqrt{\rho_{1,1}\rho_{6,6}} - \sqrt{\rho_{1,1}\rho_{7,7}} - \sqrt{\rho_{1,1}\rho_{10,10}} - \sqrt{\rho_{1,1}\rho_{11,11}} - \sqrt{\rho_{1,1}\rho_{13,13}} \quad (4)$$

where the maximisation is over all *local filter* (LF) operations, $\rho \mapsto (F_1 \otimes F_2 \otimes F_3 \otimes F_4)\rho(F_1^\dagger \otimes F_2^\dagger \otimes F_3^\dagger \otimes F_4^\dagger)$, where the F_i are arbitrary 2-by-2 matrices. The set LF includes local unitaries as a small proper subset, and is

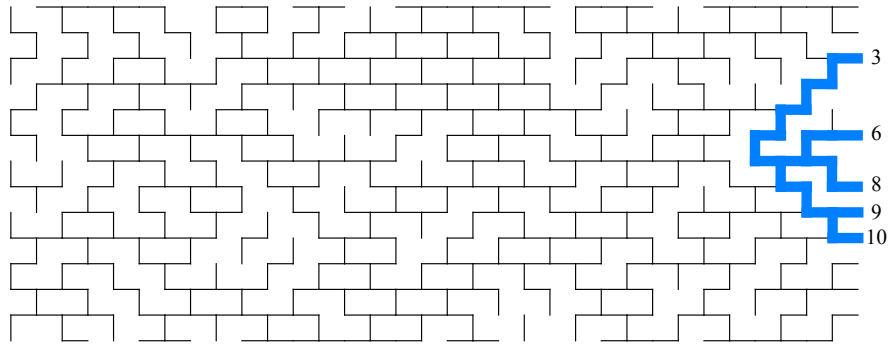


FIG. 6. **Entanglement graphs with 4 spins.** The time-evolution history for a $L = 14$ circuit at $p = 0.3$. The complete minimal spanning graph involving spins $(3, 6, 8, 9, 10)$ is shown.

thus more powerful. When $W_4 > 0$, we conclude that the system has 4-party GME. If $W_4 = 0$ (within machine precision), we cannot conclude anything, and other methods need to be used. Note that $W_4 < 0$ is not possible since LF can always bring the state into the zero matrix. This criterion was obtained from the 4-spin W state $|W_4\rangle = \frac{1}{\sqrt{2}}(|0001\rangle + |0010\rangle + |0100\rangle + |1000\rangle)$. For instance, the first 6 terms in (4) are the norms of the off-diagonal elements of ρ in the upper triangle that correspond to the non-vanishing matrix entries of $|W_4\rangle\langle W_4|$.

-
- [1] B. Skinner, J. Ruhman, and A. Nahum, *Phys. Rev. X* **9**, 031009 (2019).
- [2] Y. Li, X. Chen, and M. P. A. Fisher, *Phys. Rev. B* **98**, 205136 (2018).
- [3] Y. Li, X. Chen, and M. P. A. Fisher, *Phys. Rev. B* **100**, 134306 (2019).
- [4] C.-M. Jian, Y.-Z. You, R. Vasseur, and A. W. W. Ludwig, *Phys. Rev. B* **101**, 104302 (2020).
- [5] A. Chan, R. M. Nandkishore, M. Pretko, and G. Smith, *Phys. Rev. B* **99**, 224307 (2019).
- [6] A. Zabalo, M. J. Gullans, J. H. Wilson, S. Gopalakrishnan, D. A. Huse, and J. H. Pixley, *Phys. Rev. B* **101**, 060301 (2020), [arXiv:1911.00008 \[cond-mat.dis-nn\]](#).
- [7] M. P. Fisher, V. Khemani, A. Nahum, and S. Vijay, *Annual Review of Condensed Matter Physics* **14**, 335 (2023).
- [8] G. Vidal and R. F. Werner, *Phys. Rev. A* **65**, 032314 (2002).
- [9] M. B. Plenio, *Phys. Rev. Lett.* **95**, 090503 (2005).
- [10] B. Shi, X. Dai, and Y.-M. Lu, “Entanglement negativity at the critical point of measurement-driven transition,” (2021), [arXiv:2012.00040 \[cond-mat.stat-mech\]](#).
- [11] G. Perez and W. Witczak-Krempa, “The fate of entanglement,” (2024), [arXiv:2402.06677 \[quant-ph\]](#).
- [12] P. Calabrese, J. L. Cardy, and E. Tonni, *Phys. Rev. Lett.* **109**, 130502 (2012), [arXiv:1206.3092](#).
- [13] P. Calabrese, J. L. Cardy, and E. Tonni, *J. Stat. Mech.* . P02008 (2013), [arXiv:1210.5359](#).
- [14] G. Perez and W. Witczak-Krempa, “Are fermionic quantum critical systems more entangled?” (2024), [arXiv:2310.15273 \[cond-mat.str-el\]](#).
- [15] G. Di Francesco, B. Spagnolo, D. Valenti, and A. Carollo, (2023), [arXiv:2302.10132 \[quant-ph\]](#).
- [16] A. Paviglianiti and A. Silva, *Phys. Rev. B* **108**, 184302 (2023), [arXiv:2302.06477 \[quant-ph\]](#).
- [17] A. Nahum, J. Ruhman, S. Vijay, and J. Haah, *Phys. Rev. X* **7**, 031016 (2017).
- [18] O. Gühne and M. Seevinck, *New Journal of Physics* **12**, 053002 (2010).
- [19] S. M. Giampaolo and B. C. Hiesmayr, *Phys. Rev. A* **88**, 052305 (2013).
- [20] S. M. Giampaolo and B. C. Hiesmayr, *New Journal of Physics* **16**, 093033 (2014).
- [21] T.-T. Wang, M. Song, L. Lyu, W. Witczak-Krempa, and Z. Y. Meng, “Entanglement microscopy: Tomography and entanglement measures via quantum monte carlo,” (2024), [arXiv:2402.14916 \[cond-mat.str-el\]](#).
- [22] V. Vedral, M. B. Plenio, M. A. Rippin, and P. L. Knight, *Phys. Rev. Lett.* **78**, 2275 (1997).
- [23] J. Riddell and S. J. Avakian, *The Qbit++ book* (2024).